



Multilevel Mechanisms Driving Intraplate Volcanism in Central Mongolia Revealed by Adjoint Waveform Tomography of Receiver Function and Ambient Noise Data

Mijian Xu ^{a,b}, Kai Wang ^c, Jing Chen ^a, Jing He ^d, Qinya Liu ^{b,e}, Yiduo Liu ^f, Zhouchuan Huang ^g, Ping Tong ^{a,h,i,*}

^a Division of Mathematical Sciences, School of Physical and Mathematical Sciences, Nanyang Technological University, Singapore, Singapore

^b Department of Physics, University of Toronto, Toronto, Canada

^c School of Earth and Space Sciences, University of Science and Technology of China, Hefei, China

^d National Institute of Natural Hazards, Ministry of Emergency Management of China, Beijing, China

^e Department of Earth Sciences, University of Toronto, Toronto, Canada

^f Key Laboratory of Mountain Hazards and Surface Processes, Institute of Mountain Hazards and Environment, Chinese Academy of Sciences, Chengdu, China

^g School of Earth Sciences and Engineering, Nanjing University, Nanjing, China

^h Earth Observatory of Singapore, Nanyang Technological University, Singapore, Singapore

ⁱ Asian School of the Environment, Nanyang Technological University, Singapore, Singapore

ARTICLE INFO

Keywords:

Adjoint tomography
Receiver function
Ambient noise
Intraplate volcano
Central Mongolia

ABSTRACT

The genesis of the Cenozoic intraplate volcanism in Central Mongolia, characterized by sustained and low-volume eruptions remains debated due to the lack of a comprehensive model to interpret the Cenozoic volcanic activities. Here, we introduce a high-resolution 3D velocity model of the Hangay Dome, using a novel joint method which combines receiver function adjoint tomography and ambient noise adjoint tomography. The small-scale low-velocity zones in the crust and uppermost mantle reveal a crustal magma reservoir and partially molten subcontinental lithospheric mantle (SCLM). Melt fraction estimation indicates low-degree partially molten crust and SCLM. Combining previous geophysical and geochemical observations, we suggest that the volcanism in the Hangay Dome is driven by multilevel mechanisms. The remnant Mesozoic volatiles triggered upper mantle upwelling. This upwelling accumulated in the asthenosphere, heating the SCLM, and prompted its low-degree partial melting. The molten SCLM caused local lithospheric thinning and facilitated the magmatic underplating in the lower crust, eventually leading to the formation of the crustal magma reservoir.

1. Introduction

Intraplate volcanoes, which develop within the continents, usually have complex origins. The convective upper mantle may potentially contribute to the formation of typical intraplate volcanoes following some end-member models, including edge-driven convection (King and Anderson, 1998; Mather et al., 2020), downwelling drips (Elkins-Tanton, 2007), and rapid asthenospheric shear (Conrad et al., 2011). The intraplate volcanoes in the Hangay Dome (Tariat and Orkhon Volcano in Fig. 1a), located in central Mongolia, are featured by Oligocene to Holocene basalts resulting from sustained low-volume volcanic activities (Barry et al., 2007; Cunningham, 2001). However, the basalts in Central Mongolia (including Hangay Dome) are primarily

composed of a mixture of depleted mantle (DMM) and enriched mantle (EM1) components. This composition is significantly different from that of other typical intraplate volcanoes, which are formed by upper mantle convection and display an enriched mantle (EM1/EM2) signature (Li et al., 2016; Mather et al., 2020). Moreover, the Hangay Dome is far away from the Pacific subduction zone and exhibits low asthenospheric shearing (Conrad et al., 2011). Thus, current end-member models appear inadequate in interpreting the origins of Hangay intraplate volcanoes. It is crucial to comprehensively consider the temporal and spatial complexities when discussing the formation of volcanic activities in the Hangay region.

The Hangay Dome has experienced a complicated tectonic history with significant magmatic activity, including the closure of the Paleo-

* Corresponding author.

E-mail address: tongping@ntu.edu.sg (P. Tong).

Asian Ocean in the Paleozoic (Sengör et al., 1993), the closure of the Mongol-Okhotsk Ocean in the Mesozoic (Van Der Voo et al., 2015; Wang et al., 2022a), and the tectonic reactivation due to the far-field India-Asia collision in the Cenozoic (Barry, 2003; Tapponnier and Molnar, 1979). Regarding the cause of the intraplate volcanoes in the Hangay Dome, continental seismic tomography reported low-velocity anomalies extending from the mantle transition zone to the uppermost mantle (Chen et al., 2015), supporting the hypothesis that volcanoes originate from upper mantle upwelling (Windley and Allen, 1993). On the other hand, the removal of lithosphere triggered by delamination or dripping beneath the Hangay Dome is suggested by regional geophysical imaging results, unveiling low-velocity and high-conductivity anomalies in the uppermost mantle beneath the Hangay dome with a lateral extension of ~ 400 – 500 km (Comeau et al., 2018; Feng, 2021; Huang and Zhao, 2022; Wang et al., 2022b), along with a thinning lithosphere (Zhao et al., 2021). Nevertheless, Cenozoic basalts, characterized by a blend of depleted and enriched mantle signature (Hunt et al., 2012; Togtokh et al., 2019), indicate that the origins of magma involve a mixture of recycled oceanic crust and lithospheric mantle. Meanwhile, Hunt et al. (2012) propose that magmatic activity originated from

small-scale, low-degree partial melting and became increasingly dominated by molten lithosphere from the Oligocene to the Holocene, as it was heated by underlying asthenospheric upwelling. Although the molten lithosphere has been sustainably heating, the shallow crust lacks significant felsic magma reservoir (Comeau et al., 2022). In addition, gravity data and receiver function analyses have revealed a thickened crust beneath the Orkhon Volcano (Guy et al., 2024; Petit et al., 2008), implying crustal underplating of mafic magma. In summary, the tectonic and magmatic evolution of the Hangay Dome is closely tied to its geological history, mantle upwelling, and lithospheric dynamics, with volcanic activity shaped by contributions from both recycled oceanic crust and lithospheric melting. However, a comprehensive model capable of simultaneously interpreting multiple types of observations is still absent. Therefore, high-resolution seismic imaging of the crust and lithospheric mantle becomes essential for gaining a comprehensive understanding of the volcanic origins and magma transportation process in the Hangay Dome region.

Utilizing dense seismic stations and waveform adjoint tomography methods can effectively reveal detailed subsurface velocity structures. In a previous study, we developed an innovative receiver function adjoint

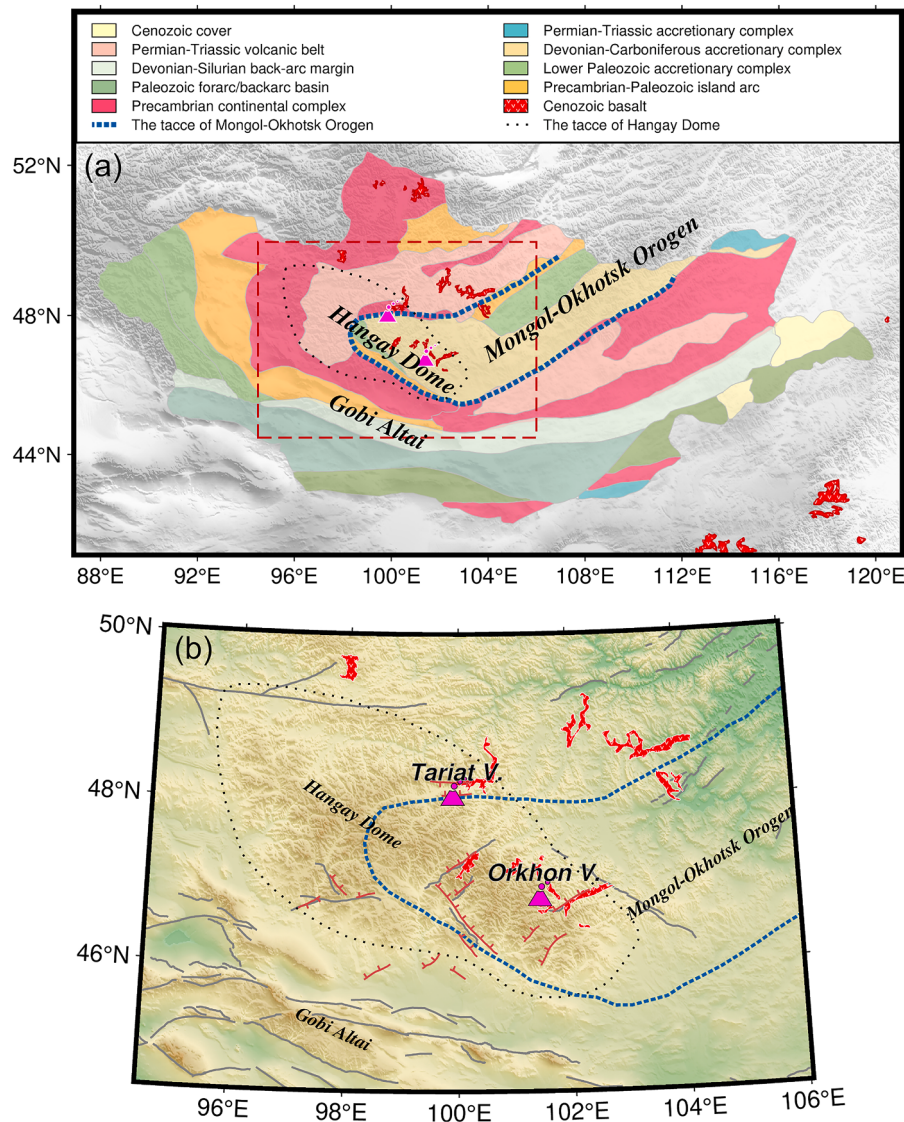


Fig. 1. (a) Tectonic map view of Mongolia (modified from (Li et al., 2022)). The dashed red box denotes the study region. The volcano symbols denote the Tariat and Orkhon volcanoes. The dotted black line denotes the trace of Hangay Dome. The dashed blue line denotes the trace of Mongol-Okhotsk Orogen. (b) A zoomed-in topographic map of Hangay Dome and adjacent regions. The gray lines denote active faults, while the brown lines specifically represent active normal faults (Cunningham, 2001).

tomography (RFAT) method that can effectively resolve lateral heterogeneities in S-wave velocities (Xu et al., 2023). However, its lateral resolution may be compromised in areas where stations are too sparse to sample the complex scattering wavefield. Ambient noise surface wave adjoint tomography (ANAT) has demonstrated efficacy in imaging S-wave velocities with high lateral resolution (Chen et al., 2014; Wang et al., 2018). Therefore, by integrating ANAT to compensate for the limitations of RFAT in lateral resolution, we can obtain higher-resolution S-wave velocity structures in the crust and uppermost mantle than using one approach alone. In this study, we propose an adjoint waveform tomography method that jointly inverts receiver functions and ambient noise data (JointAT). We apply this method to the dense seismic array in the Hangay Dome (Meltzer et al., 2019) to illustrate small-scale low velocity anomalies beneath volcanoes. These new findings reveal the evolution of Cenozoic volcanism in central Mongolia, enhancing our understanding of the origins of intraplate volcanoes.

2. Database

In this study, we utilize seismic waveform data from 66 broadband stations provided by the IRIS Data Management Center of Seismological Facility for the Advancement of Geoscience spanning from June 2012 to April 2014 (Fig. 2a). These stations cover the Hangay Dome and extend across it through two dense linear arrays oriented from north to south.

2.1. Receiver functions

For P-wave receiver function (PRF) calculation, we select teleseismic earthquakes with an epicentral distance ranging from 30° – 90° and a magnitude larger than 5.8. A total of 445 events are employed for subsequent processing for PRFs. A previously established workflow is used to pre-process seismic records (Xu et al., 2020). The PRFs with a Gaussian factor of 1.0 (cut-off frequency of ~ 0.48 Hz) are calculated by using the iterative deconvolution method (Ligorria and Ammon, 1999). A total of 10,465 PRFs are retained following a manual quality control using Seispy software (Xu and He, 2023).

To enhance the signal-to-noise ratio of PRFs, we classify events to 28 groups as virtual sources using the agglomerative clustering method (Murtagh and Legendre, 2014), based on analogous back-azimuths and ray parameters (Fig. 2b). For each station, the PRFs within the same

group are stacked in preparation for the inversion.

2.2. Ambient noise surface wave

We extract Rayleigh-wave cross-correlation functions with periods of 5–50 s from the vertical components of continuous seismic data following standard noise data processing procedures (Bensen et al., 2007). Empirical Green's functions (EGFs) are obtained by computing the reversed time derivative of the cross-correlation functions. The ray paths show good coverage over the Hangay Dome (Fig. 2a). In total, we obtain 2,143 high-quality EGFs containing Rayleigh waves from 65 virtual sources (Figure S1).

3. Methodology

Both PRFs and EGFs are sensitive to S-wave velocity in the crust and uppermost mantle. Notably, PRFs have good resolution from the Earth's surface to ~ 100 km depth (Xu et al., 2023). However, the small incidence angles of teleseismic events require a dense array to ensure adequate lateral resolution. On the other hand, ambient noise surface waves have good resolution in the crust and uppermost mantle ($< \sim 50$ km), but their sensitivity diminishes at greater depths. Therefore, these two datasets, providing complementary sensitivity, can be combined to determine the S-wave velocity in the crust and uppermost mantle with the innovative JointAT method.

3.1. Individual inversion of PRFs and EGFs

The JointAT method combines RFAT and ANAT to invert PRFs and EGFs simultaneously. This can be achieved by defining different objective functions for each inversion process. RFAT optimizes model parameters by minimizing the misfits between the observed and synthetic PRFs (Xu et al., 2023). The objective function of RFAT with a given time window from t_1 to t_2 is expressed as

$$\chi_{\text{PRF}} = \frac{1}{2} \sum_{i=1}^N \int_{t_1}^{t_2} W_i \|s_{rf}(t) - d_{rf}(t)\|^2 dt, \quad (1)$$

where s_{rf} and d_{rf} are synthetic and observed PRF, respectively. W_i is the

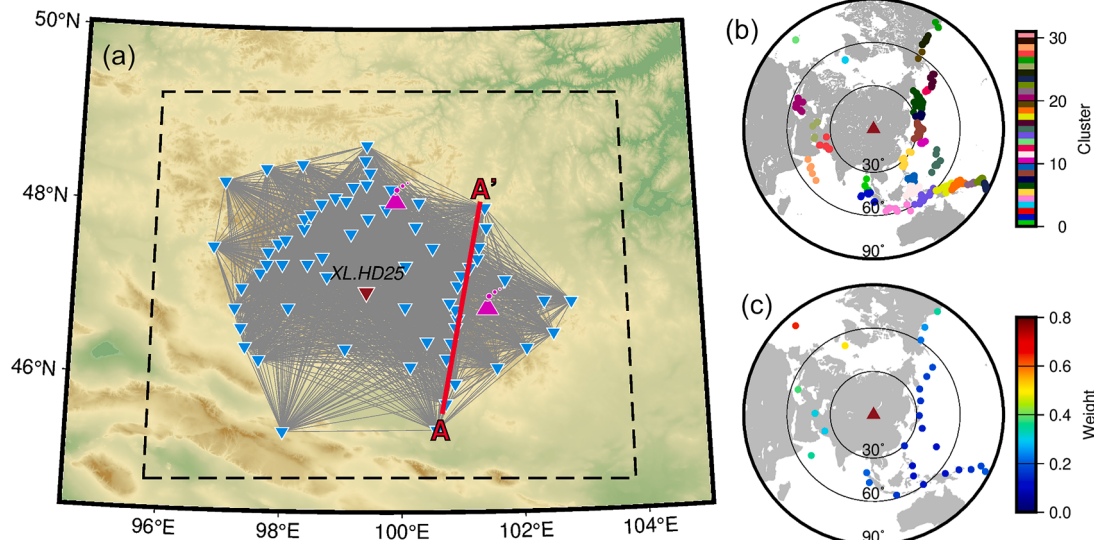


Fig. 2. (a) Stations (blue triangles) for measuring objective functions of P-wave receiver functions (PRFs) and Empirical Green's functions (EGFs). Gray lines denote the ray path coverage of the EGFs. The red line denotes profile AA'. The dashed box denotes the region of computational domain. (b) Earthquakes used for PRF calculation. Events are grouped into clusters, each represented by the same color. (c) Locations of virtual events for the PRFs. Colors denote event weights defined in equation (5) and determined using the geographical weighting method (Ruan et al., 2019).

weight of the i^{th} PRF among N measurements.

For ANAT, we minimize the phase misfit between EGFs and synthetic Green's functions measured on vertical components as

$$\chi_{EGF} = \frac{1}{2} \sum_{i=1}^N \int \frac{h_i(\omega)}{H_i} \left[\frac{\Delta T_i(\omega, \mathbf{m})}{\sigma_i} \right]^2 d\omega, \quad (2)$$

where $\Delta T(\omega, \mathbf{m})$ is a frequency-dependent travel time difference relative to model \mathbf{m} with uncertainties σ_i determined by employing a multitaper technique (Tape et al., 2010; Zhou et al., 2004). $h_i(\omega)$ is a frequency-domain window normalized by $H_i = \int_{-\infty}^{+\infty} h_i(\omega) d\omega$.

Given perturbations of Vp, Vs and density, the perturbations of the objective functions for RFAT and ANAT (Wang et al., 2021; Xu et al., 2023) have a uniform form of

$$\delta\chi = \int (K_\rho \delta \ln \rho + K_a \delta \ln \alpha + K_\beta \delta \ln \beta) d^3x, \quad (3)$$

where K_ρ , K_a , and K_β are sensitivity kernels of density, Vp, and Vs, respectively. These kernels, computed using the adjoint method (Liu and Tromp, 2006; Tromp et al., 2005), facilitate the updating of model parameters via a linearized optimization technique, such as the limited-memory BFGS method (Nocedal and Wright, 2006).

3.2. Adjoint waveform tomography integrating PRF and EGF

Due to the completely different objective functions of PRF and EGF inversions, a weighted non-dimensionalized sum of different sensitivity kernels is employed to balance their contributions. We first use a well-established workflow to calculate the individual sensitive kernels for PRFs and EGFs (Wang et al., 2018; Xu et al., 2023). Post-processing, including summation, pre-conditioning, and smoothing, is performed on these kernels. This yields the pre-conditioned gradients in the n^{th} iteration, denoted as $G_{PRF}(\mathbf{m}_n)$ for PRFs and $G_{EGF}(\mathbf{m}_n)$ for EGFs (Fig. 3), where \mathbf{m} is the model parameter vector of V_p , V_s , and ρ . Subsequently, we perform a weighted summation of the misfit gradients to obtain the descent direction of optimization, denoted as $d(\mathbf{m}_n)$:

$$d(\mathbf{m}_n) = \frac{G_{PRF}(\mathbf{m}_n)}{\|G_{PRF}(\mathbf{m}_0)\|_\infty} + \frac{G_{EGF}(\mathbf{m}_n)}{\|G_{EGF}(\mathbf{m}_0)\|_\infty}. \quad (4)$$

where $1 / \|G_{PRF}(\mathbf{m}_0)\|_\infty$ and $1 / \|G_{EGF}(\mathbf{m}_0)\|_\infty$ are the weights of PRFs and EGFs, respectively. During the initial iteration, these two datasets

are assigned equivalent contribution. However, the amplitude of pre-conditioned gradients trend to decrease as the misfit decreases with iterations. This weighted non-dimensionalized approach ensures a harmonized contribution from both datasets towards the optimization direction.

3.3. Workflow of JointAT

In this study, we employ SPECFEM3D to simulate synthetic teleseismic waveforms and surface wave SGFs in a domain from 95.8° E to 103.8° and 44.8° N to 49.25° N with surface topography in consideration (Komatsch and Vilotte, 1998). The domain is discretized to $112 \times 96 \times 24$ elements, with each element having a size of ~ 5 km in one direction in 3D space (Fig. 4a). A reference velocity model is introduced, with the S-wave velocity following a modified IASP91 model in which the Moho and Conrad adjusted according to Feng (2021) and He et al. (2016). The Moho is adjusted from 35 km to 50 km, and the Conrad is shifted from 15 km to 30 km. Subsequently, Gaussian smoothing is applied to this velocity model to derive the initial Vs model for tomography (Fig. 4b). These steps generate an initial model that is relatively close to the true model, which help to reduce the non-linearity and avoid cycle skipping. Although the initial model is adjusted according to the Moho depth, the Moho interface is not explicitly included as a model parameter for the inversion to prevent trade-offs between the perturbations of velocity and the interface. The P-wave velocity and density of the initial model are inferred from empirical relationships (Brocher, 2005).

For measuring the objective function of PRFs, we simulate teleseismic waveforms from 28 virtual sources by employing the SEM-FK method with plane wave injection (Tong et al., 2014). The take-off angle θ of each virtual source is calculated by $\theta = \arcsin(p/V_p)$ (Monteiller et al., 2020), where p is the ray-parameter and V_p is the P-wave velocity at the bottom of the SEM domain. The synthetic PRFs are calculated by deconvolving the vertical component from the radial component of synthetic waveforms using the iterative deconvolution method (Ligorria and Ammon, 1999). The misfit between synthetic and observed PRFs is measured using Equation (1), with event weights W_i (Fig. 2c) computed using the geographical weighting method (Ruan et al., 2019) given by

$$W_i^{-1} = \sum_j^N \exp \left[- \left(\frac{\Delta_{ij}}{\Delta_0} \right) \right], \quad (5)$$

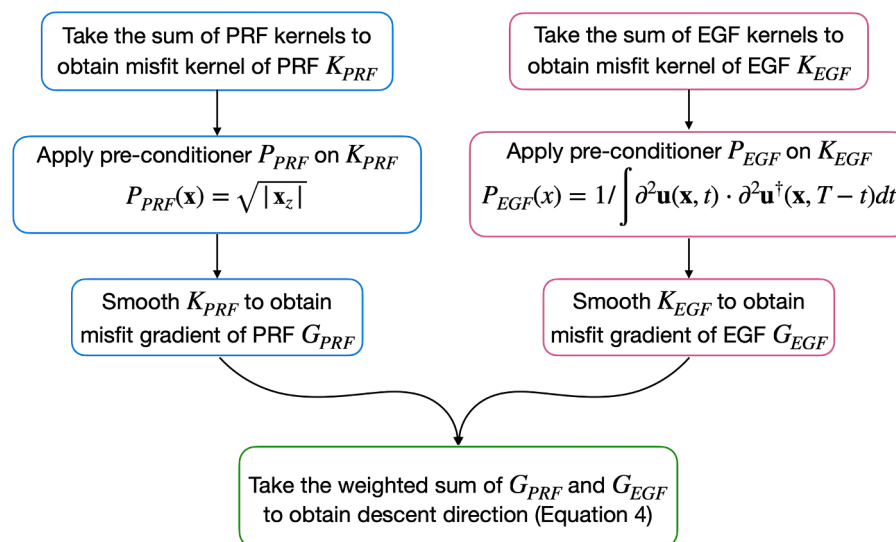


Fig. 3. Post-processing workflow for adjoint waveform tomography inverting a joint dataset of receiver function data (blue frames) and ambient noise data (red frames).

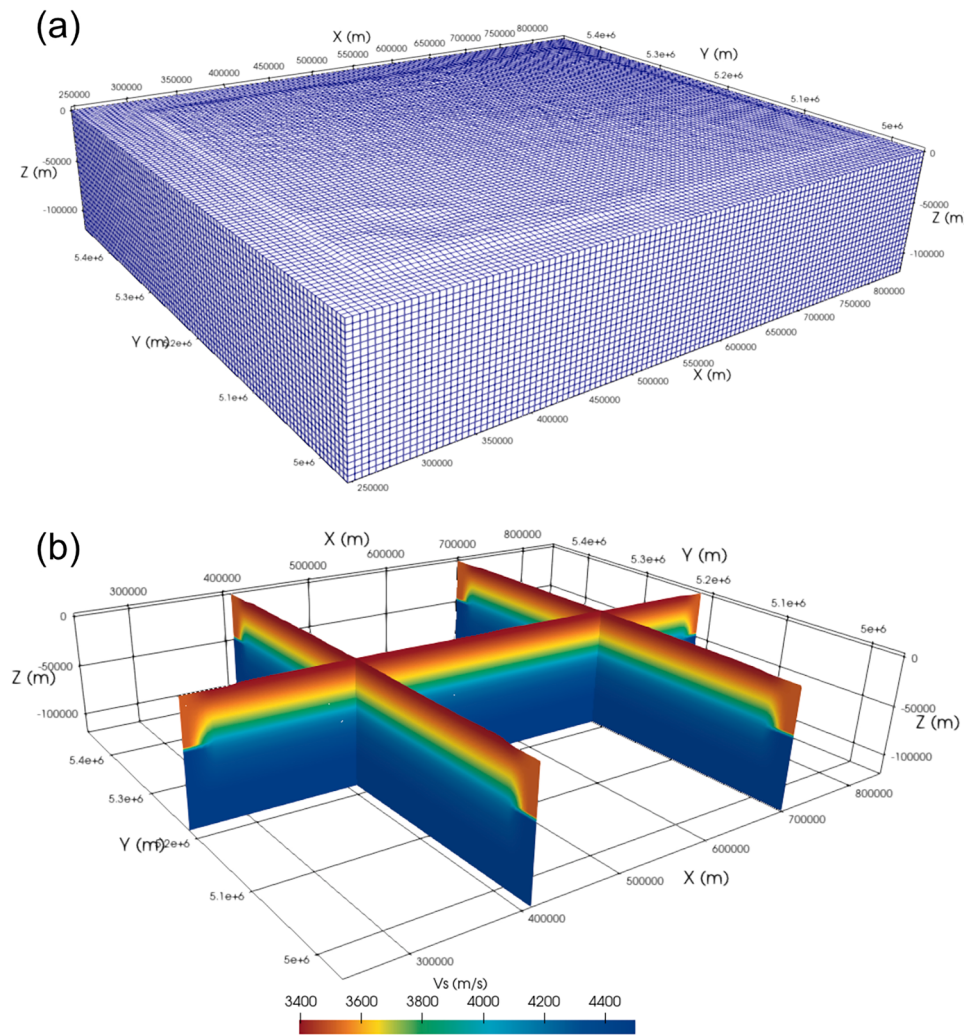


Fig. 4. (a) A chunk of mesh for forward and adjoint simulation for the study region. (b) The initial S-wave velocity model used for the jointAT.

where Δ_{ij} is the distance of each event pair. Δ_0 is a reference distance parameter, which is selected by averaging Δ_{ij} in this study.

For the ambient noise surface wave data, SGFs are simulated using vertical point-force sources with a Gaussian source time function (maximum frequency of 0.3 Hz). Both EGFs and SGFs are filtered within three narrow bands of 6 - 15s, 10 - 25s, and 20 - 35s to calculate the frequency-dependent travel time differences, as estimated using Equation (2) via the multitaper method (Tape et al., 2010; Wang et al., 2018).

The adjoint sources derived from the misfit objective functions for both PRFs and EGFs are then calculated (Wang et al., 2018; Xu et al., 2023). The sensitivity kernel related to each virtual event is computed through the interaction between the forward and adjoint wavefields (Liu and Tromp, 2006; Tromp et al., 2005). The adjoint wavefield is generated by time-reversed adjoint sources at receiver locations. Subsequently, we sum, precondition, and smooth all event kernels corresponding to both PRFs and EGFs. The preconditioner is utilized to approximate the Hessian matrix and aimed to suppress extreme sensitivities near sources and receivers, while simultaneously accelerating the convergence of inversion. For the inversion of PRFs, the preconditioner is determined by the square root of the depth (Wang et al., 2016), whereas for the inversion of EGFs, it is defined as the vector dot product of the forward and adjoint accelerations (Zhu et al., 2015) (Fig. 3). To further regularize the objective function, a Gaussian function is applied to smooth the summed and pre-conditioned kernels (Tape et al., 2010). The descent direction for further optimization is then constructed by

taking a weighted sum of these smoothed kernels (Fig. 4). We employ the limited-memory BFGS algorithm for optimization (Nocedal and Wright, 2006), and a line search method to determine the optimal step length for model updating (Zhu et al., 2015). After ten iterations, we obtain the final model M10 when the misfit of PRFs decreases by 50%, and the misfit of EGFs decreases by over 60% (Fig. 5a). The waveform fit of the synthetics to the observed PRFs and the EGFs has been significantly improved in the final model compared to the initial model (Figs. 5b, 5c and S2 -S7).

4. Results

4.1. Resolution tests

We conduct resolution tests using JointAT to evaluate the resolution of the selected data, comparing the results with those obtained using ANAT and RFAT, following a previously established strategy (Van Herwaarden et al., 2023; Xu et al., 2023). We initially introduce perturbations to the final model M10 as the perturbed model R00. Subsequently, we invert the true data, including both the EGF and PRF, starting from R00 to recover M10. Theoretically, the recovered model should converge to M10, as it represents the optimal solution. However, in practice, achieving this ideal state is constrained by the distribution of stations and the presence of data noise. Thus, the resolution can be assessed by measuring the deviations of the perturbed model (R00) from the recovered model. This resolution evaluation strategy has several

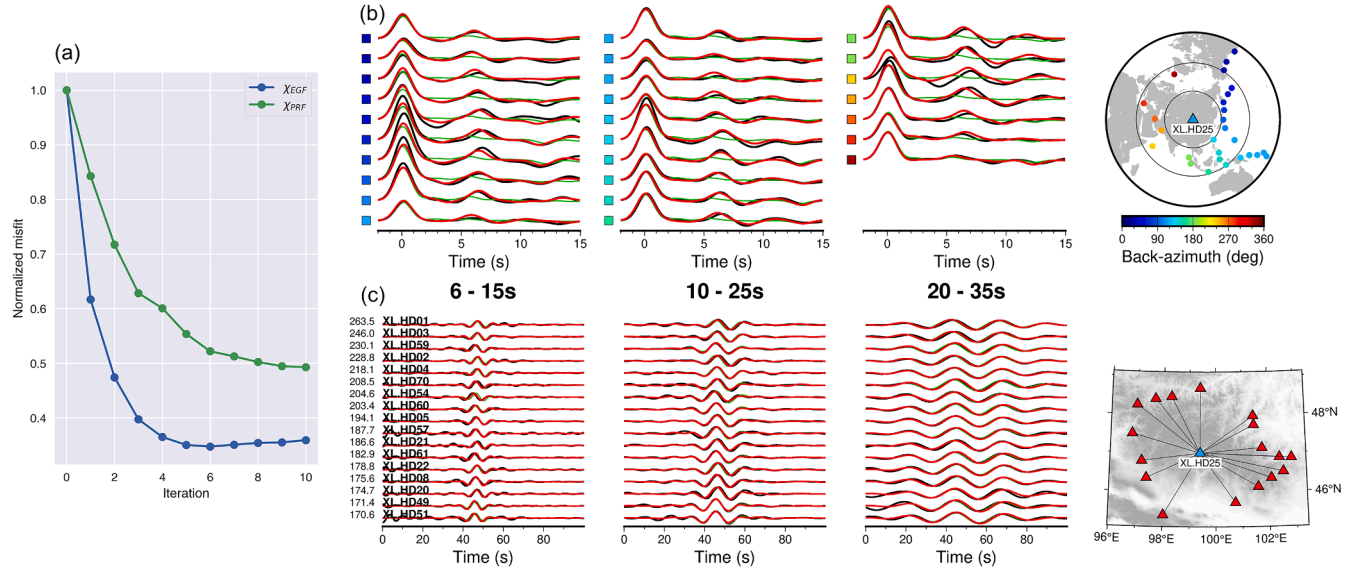


Fig. 5. (a) Normalized misfit reduction of P-wave receiver function data (green line) and ambient noise data (blue line) over iterations. (b) Waveform fitting at station XL.HD25 for receiver functions. The black line represents the observed data, the green line represents the synthetic data derived from the initial model, and the red line represents the synthetic data derived from the final model. Colored squares denote back-azimuth of events shown in the right subfigure. (c) Waveform fitting of partial waveforms from a virtual source at XL.HD25 for ambient noise data, focusing on period bands of 6 – 15s (left panel), 10 – 25s (middle panel), and 20 – 35s (right panel). Black and red lines are consistent with those in (b). Numbers represent distance. Location of each station is shown in the right subfigure.

benefits compared to previous methods (checkerboard test and approximate Hessian analysis): first, the resolution test includes the final model that is close to the true model; second, real data with real noise is

employed as data instead of synthetic data and additional random noise; third, the resolution test takes into account the non-linearity of the objective function.

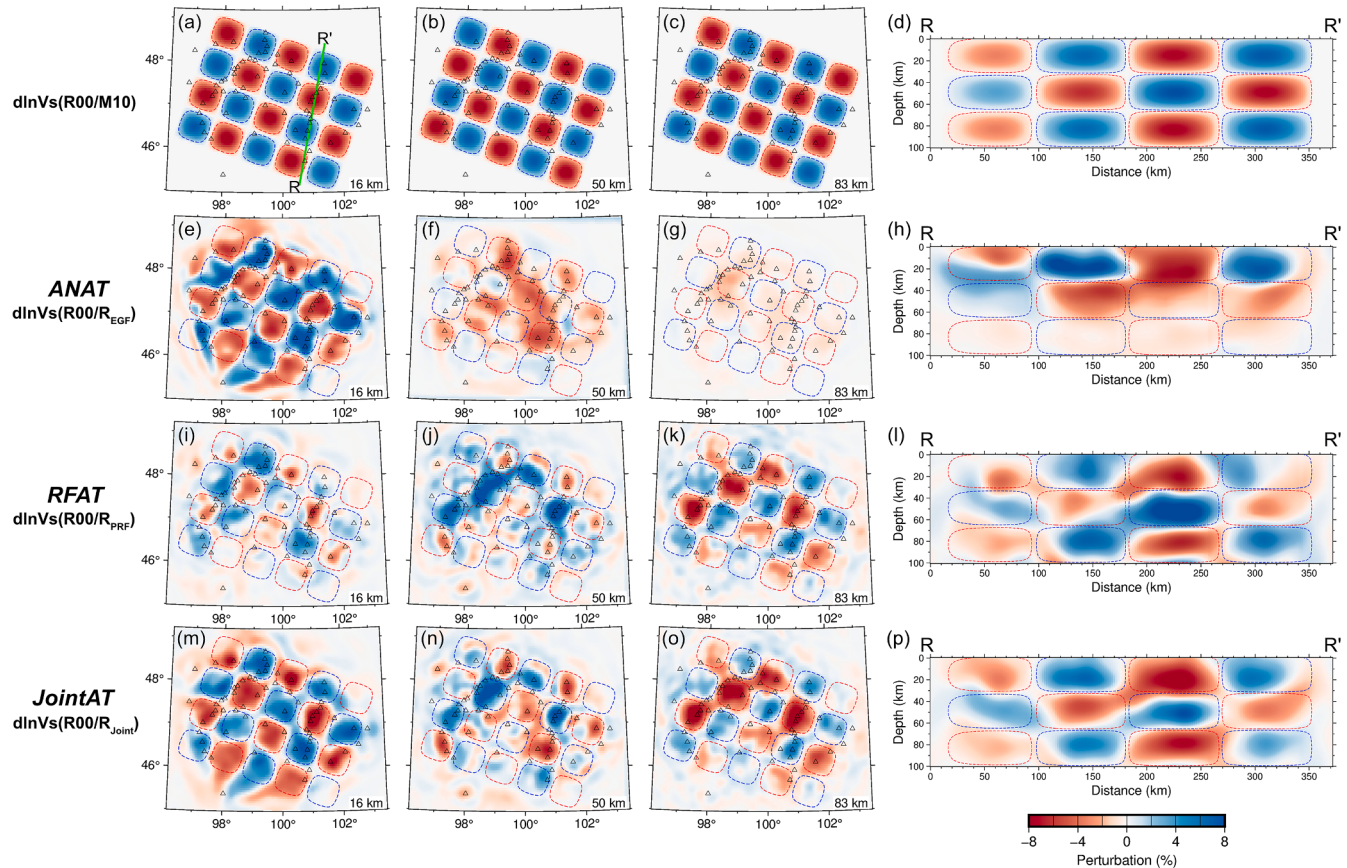


Fig. 6. Resolution tests. Perturbations of R00 relative to the final model M10 (a–d), the model R_{EGF} derived from ambient noise adjoint tomography (e–h) (ANAT), the model R_{PRF} obtained via receiver function adjoint tomography (i–l) (RFAT), and the model R_{Joint} derived from joint adjoint waveform tomography inverting receiver functions and ambient noise data (m–p) (JointAT).

In the resolution test, we introduce alternating perturbations with a maximum amplitude of 8% to M10 to generate the perturbed model R00 (Figs. 6a-6d). We then employ the ANAT, RFAT, and JointAT methods to invert the observed data starting from R00, resulting in recovered model, REGF (Figs. 6e-6h), RPRF (Figs. 6i-6l), and R_{Joint} (Figs. 6m – 6p). With respect to ANAT, REGF demonstrates superior lateral resolution in the crust, yet lacks resolution in the uppermost mantle. As for RFAT, RPRF displays commendable vertical resolution from crust to uppermost mantle, specifically under a dense linear array. JointAT acquires the complimentary resolution of ambient noise data and receiver functions. R_{Joint} has the capacity to not only resolve lateral anomalies in the crust but also illuminate anomalies under the dense linear array down to the uppermost mantle. This test suggests that the JointAT offers superior resolution compared to ANAT and RFAT used individually (Fig. 6), and can be used to achieve accurate and high-resolution results in resolving lateral heterogeneity in the crust and the uppermost mantle. However, the JointAT still presents irregular resolution due to imperfect data coverage in our study area. Consequently, our discussion will focus mainly on horizontal features within the crust and lateral heterogeneities from crust to uppermost mantle along profile AA' (Fig. 2). Additionally, two other profiles BB' and CC' (Figure S8) across the Tariat volcanoes are presented in the Supplementary materials for reference (Figures S9–S10).

4.2. Tomographic results

Our tomographic results reveal the lateral heterogeneity of S-wave velocity in the crust and uppermost mantle of the Hangay Dome as shown in map view in Fig. 7. One of the most striking features is the crustal low-velocity anomaly beneath the Hangay dome. Map views at depths of 12 km and 22 km reveal low-velocity anomalies in the upper crust of the eastern and northern parts of the dome, with S-wave

velocities of 3.35 – 3.5 km/s (Figs. 7a and 7b). These anomalies are primarily observed within the Mongol-Okhotsk Orogeny, a region where numerous basalts from the Oligocene to the Holocene associated with volcanic activities have been identified. Moreover, two significant low-velocity anomalies are observed in the middle and lower crust (CLVZ1 and CLVZ2 in Figs. 7c and 7d), exhibiting S-wave velocities of 3.4 – 3.6 km/s, significantly lower than those of neighbouring areas. In particular, the CLVZ1 extends from the upper to lower crust beneath the Orkhon volcano, aligning with the high Vp/Vs ratios of ~1.77 – 1.80 (Guy et al., 2024).

Profile AA' shows the S-wave velocity of the crust and uppermost mantle across the Orkhon volcano (Fig. 8). The imaging result reveals the CLVZ1 in the lower crust beneath the Orkhon volcano. The Moho discontinuity, determined by the maximum gradient of S-wave velocity between 35 and 62 km depth, is depressed from a depth of 43 km to 54 km, which is observed slightly to the south of the Orkhon volcano. This results in an increase in crustal thickness by 11 km. Furthermore, a mantle low-velocity zone (MLVZ) is imaged at depths of 70–100 km beneath this volcano, exhibiting S-wave velocities of 4.25 – 4.4 km/s, significantly lower than the velocity observed in the surrounding lithospheric mantle (Figs. 8a and 8b). The lithosphere-asthenosphere-boundary (LAB) is traced by the gradient of S-wave velocity between depths of 65 and 90 km, with a normalized gradient greater than 0.4. Consequently, the thickness between the LAB and the Moho, attributed to the consolidated lithospheric mantle, is less than 20 km beneath the volcanic area. The presence of low-velocity anomalies beneath the Orkhon volcano suggests that Cenozoic magmatic activity has induced lateral heterogeneities within the crust-mantle structure beneath the dome.

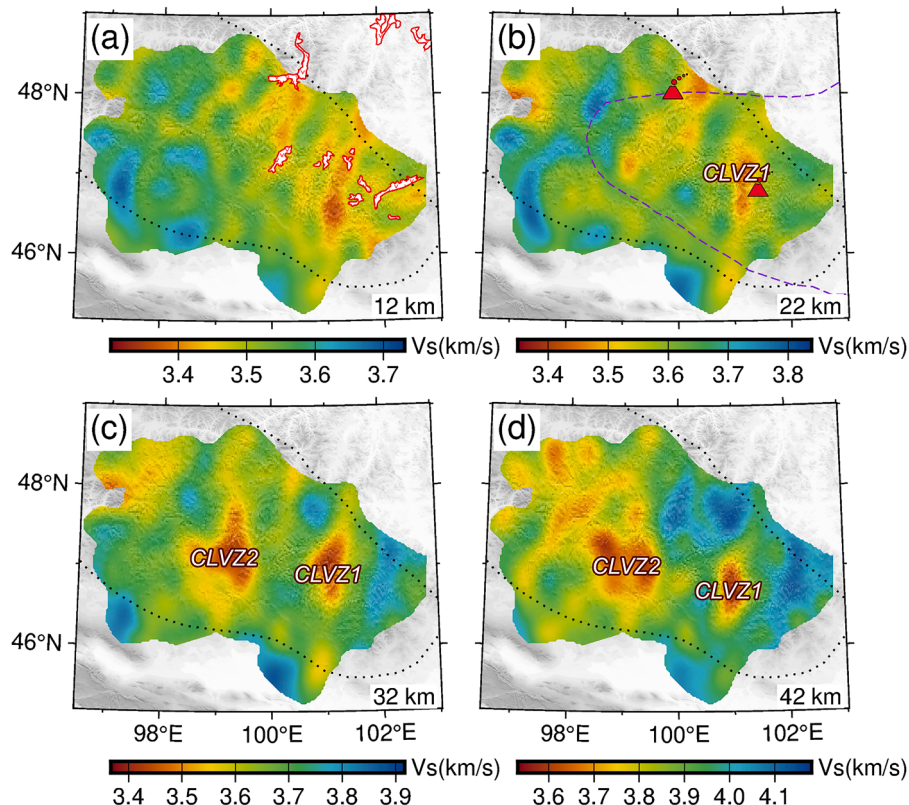


Fig. 7. Map views of S-wave velocity at depths of 12, 22, 32, and 42 km. The dotted line denotes the trace of Hangay Dome. The white zones with red boundaries in (a) represent the development of Cenozoic basalts. The dashed purple line in (b) denotes the trace of Mongol-Okhotsk Orogeny. The red volcano symbols in (b) represent the volcanoes.

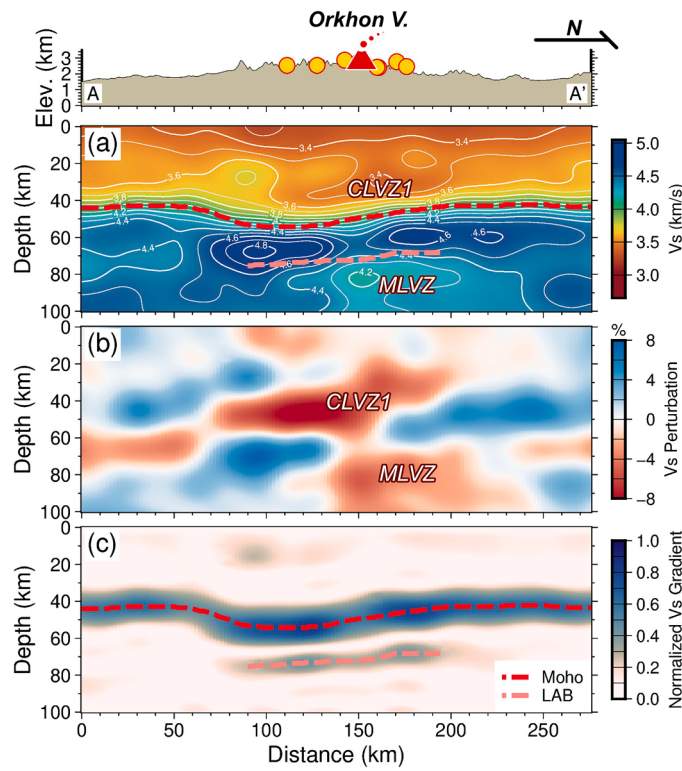


Fig. 8. Cross section of absolute Vs (a), Vs perturbations (b) and Vs gradient (c) along Profile AA', as shown in Fig. 1. The dashed red lines denote the Moho topography and the dashed pink lines denote the LAB topography. The top panel demonstrates surface topography. The yellow dots represent the locations of Cenozoic basalts. The volcano symbol represents the Orkhon Volcano.

5. Discussion

5.1. Small-scale magmatic activity and low degree of melting

Geophysical observations beneath the Hangay Dome reveal extensive low-velocity and high-conductivity anomalies within the lithospheric mantle (Chen et al., 2015; Comeau et al., 2022; Feng, 2021; Huang and Zhao, 2022; Wang et al., 2022b). These anomalies are considered to be source of Cenozoic magmatic activities. Since 33 Ma, the basaltic field observed in the Hangay Dome has been distinctly smaller in scale compared to other active intraplate volcanoes and ancient volcanic provinces (Ancuta et al., 2018; Ernst, 2014), suggesting small-scale mantle magmatic activities. The improvement in resolution has facilitated the identification of smaller-scale low-velocity anomalies in the uppermost mantle (MLVZ) beneath the Orkhon volcano, presenting a more refined structure compared to previous seismic observations (Chen et al., 2015; Feng, 2021; Wang et al., 2022b). The horizontal width of the MLVZ along profile AA' is estimated to be 150 km, based on $Vs < 4.4$ km/s (Fig. 8), indicating localized partial melting within the lithosphere mantle. This observation is consistent with geochemical studies suggesting that Holocene basaltic magma primarily results from lithospheric melting, rather than directly from asthenospheric upwelling (Ancuta et al., 2018; Hunt et al., 2012). In addition, the S-wave velocity of the MLVZ is 4.2 – 4.4 km/s, which is significantly higher than in some regions with high degrees of mantle melting, such as southern Nevada, where the velocity is 3.9 – 4.2 km/s (Rau and Forsyth, 2011). While this lithospheric melting could potentially contribute to the genesis of mantle-derived volcanic rocks, it also indicates that such small-scale, low-degree partial melting is insufficient to trigger large-scale volcanic activities.

Significant low-velocity anomalies exist within the lower crust beneath the Orkhon volcano (CLVZ1 in Figs. 7 and 8), with a distribution

pattern that strongly aligns with high-conductivity anomalies (Comeau et al., 2018), low density (Bayasgalan et al., 2005; Guy et al., 2024; Petit et al., 2008), and high average crustal Vp/Vs (Guy et al., 2024). Thus, these low-velocity anomalies are inferred to be magma reservoirs within the lower crust. Due to the presence of lithospheric melting beneath the Orkhon volcano, the solid lithospheric mantle has become extremely thin, with a thickness of less than 20 km, which provides favourable conditions for the entry of mantle melting materials into the lower crust. Gravity studies reported that in the Hangay Dome, not only a thickened crust but also the presence of crustal low-density zone is required to fit the gravitational observations (Bayasgalan et al., 2005; Petit et al., 2002). Therefore, the lithospheric melting has triggered the magmatic underplating in the lower crust, forming the crustal magma reservoir, while also contributing to crustal thickening.

The S-wave velocity in the upper crust of the Mongol-Okhotsk Orogeny is relatively low compared to adjacent regions (Figs. 7a and 7b). Nevertheless, the absolute S-wave velocity beneath the Orkhon volcano is ~3.4 km/s, which is significantly higher than that of other active volcanoes, such as the ~2.5 km/s detected beneath Yellowstone (Maguire et al., 2022) and the ~2.3 km/s detected beneath the Altiplano-Puna volcano (Ward et al., 2014). In contrast, the S-wave velocity anomaly of 3.4 – 3.5 km/s in the lower crust is close to that of ~3.4 km/s beneath Yellowstone. Furthermore, there are no distinct indications of independent magma chambers in the upper-mid crust, which is clearly different from typical active volcanoes, despite the presence of comparable magma reservoirs in the lower crust. These characteristics suggest a low degree of crustal melting, insufficient for the creation of notable magma chambers and for triggering large-scale volcanic activities.

To quantitatively assess the degree of magma melting, we have estimated the relationship between S-wave velocity and melt fraction in partially molten crustal media using Gassmann's equation (Chu et al., 2010):

$$\beta = \sqrt{\frac{\beta_0^2 \rho_s \left(1 - \frac{\phi}{\phi_c}\right)}{\rho_s(1 - \phi) + \phi \rho_f}}, \quad (6)$$

where β represents the S-wave velocity, ϕ denotes the melt fraction, and β_0 is the S-velocity of the wall rock in its solid phase. In relation to the CLVZ1, we select $\beta_0 = 3.72$ km/s as the solid phase velocity. It corresponds to the S-wave velocity of mafic granulite at 45 km depth and a temperature of 615°C (Christensen, 1996; Christensen and Mooney, 1995). The critical melt fraction, ϕ_c , is chosen to be between 30% and 35% (Scott and Kohlstedt, 2006), with a specific value of 32.5% used for our estimation. Additionally, the values of 30% and 35% are used to estimate uncertainties in the melt fraction. The densities of the solid and liquid phases, ρ_s and ρ_f , are chosen as 2.7 g/cm³ and 2.9 g/cm³, respectively. Regarding the S-wave velocity of CLVZ, the estimated melting fraction in the lower crust is 3.50%–5.57% (Fig. 9). This estimation aligns with the melting fractions of 1% – 5% indicated by geochemical measurements (Ancuta et al., 2018; Hunt et al., 2012; Meng et al., 2018). This finding suggests that the degree of melting in the crustal magma reservoir beneath the Hangay Dome is relatively low compared to other active volcanic areas, such as Clear Lake (Li et al., 2024), Altiplano-Puna (Spang et al., 2021), and northeast Japan (Chen et al., 2020). The low-degree crustal basaltic magmas beneath the Hangay Dome are unlikely to contaminate the surrounding crustal country rocks (Hunt et al., 2012; Meng et al., 2018). In addition, although the S-wave velocity of the lower crustal magma reservoir at Yellowstone is comparable (Maguire et al., 2022), the scale of the magma reservoir at Yellowstone far exceeds that of the Hangay Dome (Kelbert et al., 2012). This significant difference in scale accounts for the presence of a silicic magma chamber in Yellowstone's upper crust, which is absent in the Hangay Dome. Volcanic studies suggest that producing one unit volume of silicic rhyolite requires five times that

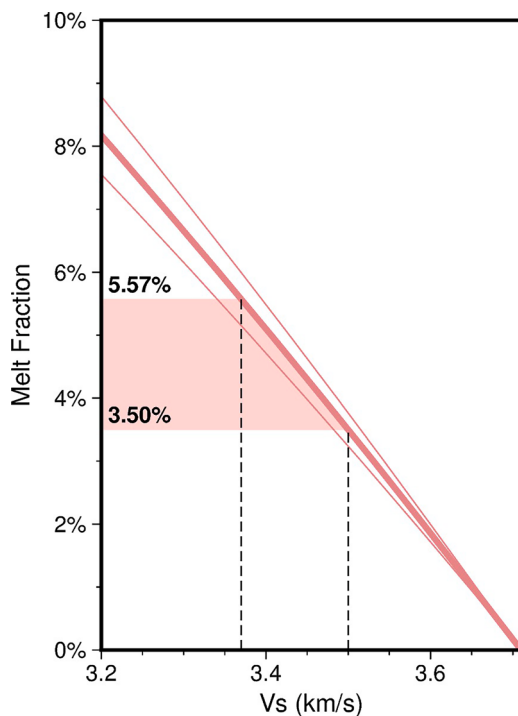


Fig. 9. Relationship between S-wave velocity and melt fraction in the lower crust (a) and lithospheric mantle (b). The thin lines represent the upper and lower boundaries of melt fraction, based on critical melt fractions set at 30% and 35%.

volume of basalt (Barker et al., 2020). Thus, the small scale and low degree of melting in the Hangay Dome lead to an absence of silicic magma and magma chambers in the upper and middle crust (Fig. 8). As a result, magma transport within the upper crust is mainly controlled by fractures (Rubin, 1995). The far-field effects of the Cenozoic Indo-Asian collision may have activated these fractures, causing normal faults that facilitate the transportation of mafic magma within the crust (Cunningham, 2001). Consequently, the small-scale partial melting and low melting fraction provide compelling evidence for the low-volume volcanism observed in the Hangay Dome.

5.2. Multilevel Cenozoic magmatic system

Current end-models for the formation of the Cenozoic Hangay Volcanoes, which are supported by regional geophysical imaging results, propose mechanisms such as lithosphere delamination and mantle upwelling (Hunt et al., 2012; Windley and Allen, 1993), which have improved our understanding of the deep origins of magma. However, due to the resolution limitations of previous imaging, these models are inadequate in providing a comprehensive interpretation for the small-scale partial melting with low melting degrees. In contrast to these end-member models, the diversity of isotopic geochemical components of the Cenozoic basalts in the Hangay Dome show clear evidence of influence from both depleted and enriched mantle components (Hunt et al., 2012; Kourim et al., 2021; Togtokh et al., 2019). This suggests that, in addition to the upwelling of primordial mantle materials, volatiles from crustal recycling play a critical role in magma genesis. Consequently, this indicates that the Cenozoic magma activity is a complex process that cannot be fully described by a simple end-member model.

Seismic tomographic studies have indicated the existence of low-velocity anomalies in the upper mantle, potentially due to upper mantle upwelling from the asthenosphere or/and the mantle transition zone (Chen et al., 2015; He et al., 2022; Huang and Zhao, 2022). As a result of the closure of the Mongol-Okhotsk Ocean in the Mesozoic,

volatiles had been transported into the bottom of the upper mantle, as evidenced by the depressed 660-discontinuity (He et al., 2022) and the basalts resulting from oceanic crustal recycling (Togtokh et al., 2019). Since the Oligocene, these remnant volatiles have contributed to the upwelling with a low melting degree from the mantle transition zone, which is supported by low-velocity zones and a thinner mantle transition zone (Chen et al., 2015; Sun et al., 2020). The upwelling results in the enriched mantle components in the basalts. The hot materials of the upwelling in the asthenosphere have been consistently heating the base of the lithosphere from the Oligocene to the Holocene, leading to a partially molten SCLM (Hunt et al., 2012). This melting process produces low-velocity anomalies in the lithospheric mantle, MLVZ, leading to further extreme thinning of the lithosphere (Fig. 8). Consequently, this molten SCLM could provide an alternate source for magma formation, exhibiting depleted geochemical characteristics.

Based on the observations from seismic imaging and other geophysical and geochemical studies, we propose a new model (Fig. 10) that unifies various observations and provides a novel understanding of the genesis of the Neogene Hangay volcano. This model reveals that the magma beneath the Hangay Dome primarily originates from three sources.

- (1) Due to the closure of the Mongol-Okhotsk Ocean during the Mesozoic, a large amount of volatiles are transported into the mantle transition zone (He et al., 2022; Sun et al., 2020). These residual volatiles cause the upper mantle upwelling with a low melting degree.
- (2) The upper mantle upwelling accumulates in the asthenosphere, heating the SCLM, leading to localized low-degree partial melting and further thinning of the lithosphere.
- (3) The magmas originating from the upper mantle inject into the lower crust through the thinned lithosphere, resulting in crustal magmatic underplating and the subsequent formation of a crustal magma reservoir.

Due to the small scale and low degree of melting, this process leads to the sustained and low-volume eruption of magma, giving rise to low-intensity volcanoes and low-volume magmatic activities.

6. Conclusions

In this study, we develop an innovative adjoint waveform tomography method which jointly inverts receiver function and ambient noise data and apply it to demonstrate the process of Cenozoic magmatic transport beneath intraplate volcanoes of Central Mongolia. This advanced technique integrates the vertical sensitivity of receiver functions with the horizontal sensitivity of ambient noise data, significantly enhancing the robustness and resolution of seismic imaging in the lithospheric scale. The new velocity structure imaging reveals partial melting in the SCLM and mid-lower crust. However, we observed no evidence of a magma chamber in the upper crust, suggesting a unique magmatic system compared to more typical volcanic regions. By computing the melt fraction and integrating regional tomographic and isotopic observations, we suggest that Cenozoic magmatism in Central Mongolia is driven by multiple levels, including upper mantle upwelling, low-degree partial melting of the SCLM, and lower crustal magma underplating. The closure of the Mesozoic Mongol-Okhotsk Ocean results in the transportation of volatiles to the bottom of the upper mantle. These residual volatiles have triggered mantle upwelling, leading to small-scale partial melting in the SCLM and thinning of the lithosphere since the Oligocene. As a result, magma is injected into the lower crust, causing localized underplating and crustal thickening. However the small-scale magma reservoir and its low-degree melting prevent the formation of significant magma chambers in the upper crust. Conversely, the movement of magma through the crust is predominantly controlled by fractures, and insufficient pressure accumulation results in

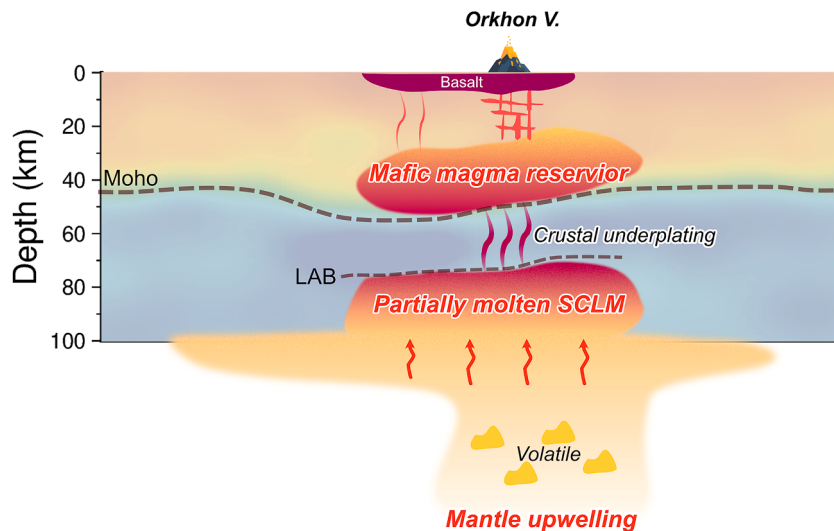


Fig. 10. Schematic view of the magmatic system under the Hangay Dome along profile AA'. The background is the S-wave velocity in Fig. 8a. The dashed gray lines denote the Moho and LAB in Fig. 8c. The abbreviation SCLM is for subcontinental lithospheric mantle.

sustained and low-volume eruptions at the Hangay Dome volcanoes from Oligocene to Holocene.

CRediT authorship contribution statement

Mijian Xu: Writing – original draft, Software, Methodology, Investigation, Formal analysis, Data curation. **Kai Wang:** Writing – review & editing, Software, Methodology. **Jing Chen:** Writing – review & editing, Validation, Methodology. **Jing He:** Investigation, Funding acquisition, Formal analysis, Data curation. **Qinya Liu:** Writing – review & editing, Supervision, Conceptualization. **Yiduo Liu:** Writing – review & editing. **Zhouchuan Huang:** Writing – review & editing. **Ping Tong:** Writing – review & editing, Supervision, Project administration, Funding acquisition, Conceptualization.

Declaration of competing interest

The authors declare that they have no known competing financial interests or personal relationships that could have appeared to influence the work reported in this paper.

Acknowledgements

This study is funded by Minister of Education, Singapore, under its MOE AcRF Tier-2 Grant (MOE-T2EP20122-0008) and its MOE AcRF Tier-1 Thematic Grant (RT12/22). This work is also funded by the National Natural Science Foundation of China (Grant Number 42074102). We thank the helpful discussion with Prof. Laicheng Miao. The raw waveform data can be downloaded from the Seismological Facility for the Advancement of Geoscience (<https://www.iris.edu/hq/>). The receiver functions are calculated by the Seispy (Xu and He, 2023). The forward and adjoint simulation are computed by SPECFEM3D (Komatitsch and Tromp, 2002a, 2002b).

Supplementary materials

Supplementary material associated with this article can be found, in the online version, at [doi:10.1016/j.epsl.2024.119137](https://doi.org/10.1016/j.epsl.2024.119137).

Data availability

Data will be made available on request.

References

- Ancuta, L.D., Zeitler, P.K., Idleman, B.D., Jordan, B.T., 2018. Whole-rock 40Ar/39Ar geochronology, geochemistry, and stratigraphy of intraplate Cenozoic volcanic rocks, central Mongolia. *GSA Bull* 130, 1397–1408. <https://doi.org/10.1130/B31788.1>.
- Barker, S.J., Rowe, M.C., Wilson, C.J.N., Gamble, J.A., Rooyakkers, S.M., Wysoczanski, R.J., Illsley-Kemp, F., Kenworthy, C.C., 2020. What lies beneath? Reconstructing the primitive magmas fueling voluminous silicic volcanism using olivine-hosted melt inclusions. *Geology* 48, 504–508. <https://doi.org/10.1130/G47422.1>.
- Barry, T.L., 2003. Petrogenesis of Cenozoic Basalts from Mongolia: Evidence for the Role of Asthenospheric versus Metasomatized Lithospheric Mantle Sources. *J. Petrol.* 44, 55–91. <https://doi.org/10.1093/petrology/44.1.55>.
- Barry, T.L., Ivanov, A.V., Rasskazov, S.V., Demeterova, E.I., Dunai, T.J., Davies, G.R., Harrison, D., 2007. Helium isotopes provide no evidence for deep mantle involvement in widespread Cenozoic volcanism across Central Asia. *Lithos* 95, 415–424. <https://doi.org/10.1016/j.lithos.2006.09.003>.
- Bayasgalan, A., Jackson, J., McKenzie, D., 2005. Lithosphere rheology and active tectonics in Mongolia: relations between earthquake source parameters, gravity and GPS measurements. *Geophys. J. Int.* 163, 1151–1179. <https://doi.org/10.1111/j.1365-246X.2005.02764.x>.
- Bensen, G.D., Ritzwoller, M.H., Barmin, M.P., Levshin, A.L., Lin, F., Moschetti, M.P., Shapiro, N.M., Yang, Y., 2007. Processing seismic ambient noise data to obtain reliable broad-band surface wave dispersion measurements. *Geophys. J. Int.* 169, 1239–1260. <https://doi.org/10.1111/j.1365-246X.2007.03374.x>.
- Brocher, T.M., 2005. Empirical Relations between Elastic Wavespeeds and Density in the Earth's Crust. *Bull. Seismol. Soc. Am.* 95, 2081–2092. <https://doi.org/10.1785/0120050077>.
- Chen, K.-X., Fischer, K.M., Hua, J., Gung, Y., 2020. Imaging crustal melt beneath northeast Japan with Ps receiver functions. *Earth Planet. Sci. Lett.* 537, 116173. <https://doi.org/10.1016/j.epsl.2020.116173>.
- Chen, M., Huang, H., Yao, H., van der Hilst, R., Niu, F., 2014. Low wave speed zones in the crust beneath SE Tibet revealed by ambient noise adjoint tomography. *Geophys. Res. Lett.* 41, 2013GL058476. <https://doi.org/10.1002/2013GL058476>.
- Chen, M., Niu, F., Liu, Q., Tromp, J., 2015. Mantle-driven uplift of Hangai Dome: New seismic constraints from adjoint tomography. *Geophys. Res. Lett.* 42, 6967–6974. <https://doi.org/10.1002/2015GL065018>.
- Christensen, N.I., 1996. Poisson's ratio and crustal seismology. *J. Geophys. Res. Solid Earth* 101, 3139–3156. <https://doi.org/10.1029/95JB03446>.
- Christensen, N.I., Mooney, W.D., 1995. Seismic velocity structure and composition of the continental crust: A global view. *J. Geophys. Res. Solid Earth* 100, 9761–9788. <https://doi.org/10.1029/95JB00259>.
- Chu, R., Helmberger, D.V., Sun, D., Jackson, J.M., Zhu, L., 2010. Mushy magma beneath Yellowstone. *Geophys. Res. Lett.* 37, 2009GL041656. <https://doi.org/10.1029/2009GL041656>.
- Comeau, M.J., Becken, M., Grayver, A.V., Käufl, J.S., Kuvshinov, A.V., 2022. The geophysical signature of a continental intraplate volcanic system: From surface to mantle source. *Earth Planet. Sci. Lett.* 578, 117307. <https://doi.org/10.1016/j.epsl.2021.117307>.
- Comeau, M.J., Käufl, J.S., Becken, M., Kuvshinov, A., Grayver, A.V., Kamm, J., Demberel, S., Sukhbaatar, U., Batmagnai, E., 2018. Evidence for fluid and melt generation in response to an asthenospheric upwelling beneath the Hangai Dome, Mongolia. *Earth Planet. Sci. Lett.* 487, 201–209. <https://doi.org/10.1016/j.epsl.2018.02.007>.

- Conrad, C.P., Bianco, T.A., Smith, E.I., Wessel, P., 2011. Patterns of intraplate volcanism controlled by asthenospheric shear. *Nat. Geosci.* 4, 317–321. <https://doi.org/10.1038/ngeo1111>.
- Cunningham, W.D., 2001. Cenozoic normal faulting and regional doming in the southern Hangay region, Central Mongolia: implications for the origin of the Baikal rift province. *Tectonophysics* 331, 389–411. [https://doi.org/10.1016/S0040-1951\(00\)00228-6](https://doi.org/10.1016/S0040-1951(00)00228-6).
- Dimitri Komatsitsch, Tromp, Jeroen, 2002b. Spectral-element simulations of global seismic wave propagation—II. Three-dimensional models, oceans, rotation and self-gravitation. *Geophysical Journal International* 150 (1), 303–318. <https://doi.org/10.1046/j.1365-246X.2002.01716.x>.
- Elkins-Tanton, L.T., 2007. Continental magmatism, volatile recycling, and a heterogeneous mantle caused by lithospheric gravitational instabilities. *J. Geophys. Res. Solid Earth* 112, 2005JB004072. <https://doi.org/10.1029/2005JB004072>.
- Ernst, R.E., 2014. Large Igneous Provinces, 1st ed. Cambridge University Press. <https://doi.org/10.1017/CBO9781139025300>.
- Feng, L., 2021. High-Resolution Crustal and Uppermost Mantle Structure Beneath Central Mongolia From Rayleigh Waves and Receiver Functions. *J. Geophys. Res. Solid Earth* 126. <https://doi.org/10.1029/2020JB021161>.
- Guy, A., Tiberi, C., Mijiddorj, S., 2024. Crustal Structures From Receiver Functions and Gravity Modeling in Central Mongolia. *J. Geophys. Res. Solid Earth* 129, e2023JB027614. <https://doi.org/10.1029/2023JB027614>.
- He, J., Wu, Q., Sandvol, E., Ni, J., Gallegos, A., Gao, M., Ulziibat, M., Demberel, S., 2016. The crustal structure of south central Mongolia using receiver functions. *Tectonics* 35, 1392–1403. <https://doi.org/10.1002/2015TC004027>.
- He, J., Xu, M., Wu, Q., Zhang, F., 2022. Hydrous Melting Driven Upwelling From the Mantle Transition Zone in the Mongolia Plateau Revealed by Receiver Function Analysis. *J. Geophys. Res. Solid Earth* 127. <https://doi.org/10.1029/2022JB024905>.
- Huang, Z., Zhao, D., 2022. Seismotectonics of Mongolia and Baikal Rift Zone Controlled by Lithospheric Structures. *Geophys. Res. Lett.* 49, e2022GL099525. <https://doi.org/10.1029/2022GL099525>.
- Hunt, A.C., Parkinson, I.J., Harris, N.B.W., Barry, T.L., Rogers, N.W., Yondon, M., 2012. Cenozoic Volcanism on the Hangai Dome, Central Mongolia: Geochemical Evidence for Changing Melt Sources and Implications for Mechanisms of Melting. *J. Petrol.* 53, 1913–1942. <https://doi.org/10.1093/petrology/egs038>.
- Kelbert, A., Egbert, G.D., deGroot-Hedlin, C., 2012. Crust and upper mantle electrical conductivity beneath the Yellowstone Hotspot Track. *Geology* 40, 447–450. <https://doi.org/10.1130/G32655.1>.
- King, S.D., Anderson, D.L., 1998. Edge-driven convection. *Earth Planet. Sci. Lett.* 160, 289–296. [https://doi.org/10.1016/S0012-821X\(98\)00089-2](https://doi.org/10.1016/S0012-821X(98)00089-2).
- Komatitsch, D., Tromp, J., 2002a. Spectral-element simulations of global seismic wave propagation—I. Validation. *Geophysical Journal International* 149 (2), 390–412. <https://doi.org/10.1046/j.1365-246X.2002.01653.x>.
- Komatitsch, D., Vilotte, J.-P., 1998. The spectral element method: An efficient tool to simulate the seismic response of 2D and 3D geological structures. *Bull. Seismol. Soc. Am.* 88, 368–392. <https://doi.org/10.1785/BSSA0880020368>.
- Kourim, F., Wang, K.-L., Beinlich, A., Chieh, C.-J., Dygert, N., Lafay, R., Kovach, V., Michibayashi, K., Yarmolyuk, V., Iizuka, Y., 2021. Metasomatism of the off-cratonic lithospheric mantle beneath Hangay Dome, Mongolia: Constraints from trace-element modelling of herzolite xenoliths. *Lithos* 400–401, 106407. <https://doi.org/10.1016/j.lithos.2021.106407>.
- Li, H.-Y., Zhou, Z., Ryan, J.G., Wei, G.-J., Xu, Y.-G., 2016. Boron isotopes reveal multiple metasomatic events in the mantle beneath the eastern North China Craton. *Geochim. Cosmochim. Acta* 194, 77–90. <https://doi.org/10.1016/j.gca.2016.08.027>.
- Li, P., Sun, M., Narantsetseg, T., Jourdan, F., Hu, W., Yuan, C., 2022. First structural observation around the hinge of the Mongolian Orocline (Central Asia): Implications for the geodynamics of orocinal bending and the evolution of the Mongol-Okhotsk Ocean. *GSA Bull.* 134, 1994–2006. <https://doi.org/10.1130/B36200.1>.
- Li, T., Wu, S., Tong, P., 2024. Multilevel transcrustal magmatic system beneath the Geysers-Clear Lake area. In: Proc. Natl. Acad. Sci., 121, e2317809121. <https://doi.org/10.1073/pnas.2317809121>.
- Ligorria, J.P., Ammon, C.J., 1999. Iterative deconvolution and receiver-function estimation. *Bull. Seismol. Soc. Am.* 89, 1395–1400. <https://doi.org/10.1785/BSSA0890051395>.
- Liu, Q., Tromp, J., 2006. Finite-Frequency Kernels Based on Adjoint Methods. *Bull. Seismol. Soc. Am.* 96, 2383–2397. <https://doi.org/10.1785/0120060041>.
- Maguire, R., Schmandt, B., Li, J., Jiang, C., Li, G., Wilgus, J., Chen, M., 2022. Magma accumulation at depths of prior rhyolite storage beneath Yellowstone Caldera. *Science* 378, 1001–1004. <https://doi.org/10.1126/science.adc0347>.
- Mather, B.R., Müller, R.D., Seton, M., Rutter, S., Nebel, O., Mortimer, N., 2020. Intraplate volcanism triggered by bursts in slab flux. *Sci. Adv.* 6, eabd0953. <https://doi.org/10.1126/sciadv.abd0953>.
- Meltzer, A., Stachnik, J.C., Sodnomsambuu, D., Munkhuu, U., Tsagaan, B., Dashdondog, M., Russo, R., 2019. The Central Mongolia seismic experiment: Multiple applications of temporary broadband seismic arrays. *Seismol. Res. Lett.* 90 (3), 1364–1376. <https://doi.org/10.1785/0220180360>.
- Meng, F., Safanova, I., Chen, S., Rioual, P., 2018. Late Cenozoic intra-plate basalts of the Greater Khingan Range in NE China and Khangai Province in Central Mongolia. *Gondwana Res* 63, 65–84. <https://doi.org/10.1016/j.gr.2018.05.009>.
- Monteiller, V., Beller, S., Plazolles, B., Chevrot, S., 2020. On the validity of the planar wave approximation to compute synthetic seismograms of teleseismic body waves in a 3-D regional model. *Geophys. J. Int.* 224, 2060–2076. <https://doi.org/10.1093/gji/ggaa570>.
- Murtagh, F., Legendre, P., 2014. Ward's Hierarchical Agglomerative Clustering Method: Which Algorithms Implement Ward's Criterion? *J. Classif.* 31, 274–295. <https://doi.org/10.1007/s00357-014-9161-z>.
- Nocedal, J., Wright, S.J., 2006. Numerical optimization. Springer series in operations research, 2nd ed. Springer, New York.
- Petit, C., Déverchère, J., Calais, E., San'kov, V., Fairhead, D., 2002. Deep structure and mechanical behavior of the lithosphere in the Hangai–Hövsgöl region, Mongolia: new constraints from gravity modeling. *Earth Planet. Sci. Lett.* 197, 133–149. [https://doi.org/10.1016/S0012-821X\(02\)00470-3](https://doi.org/10.1016/S0012-821X(02)00470-3).
- Petit, C., Tiberi, C., Deschamps, A., Déverchère, J., 2008. Teleseismic traveltimes, topography and the lithospheric structure across central Mongolia. *Geophys. Res. Lett.* 35, L11301. <https://doi.org/10.1029/2008GL033993>.
- Rau, C.J., Forsyth, D.W., 2011. Melt in the mantle beneath the amagmatic zone, southern Nevada. *Geology* 39, 975–978. <https://doi.org/10.1130/G32179.1>.
- Ruan, Y., Lei, W., Modrak, R., Örvurhan, R., Bozdag, E., Tromp, J., 2019. Balancing unevenly distributed data in seismic tomography: a global adjoint tomography example. *Geophys. J. Int.* 219, 1225–1236. <https://doi.org/10.1093/gji/ggz356>.
- Rubin, A.M., 1995. Propagation of Magma-Filled Cracks. *Annu. Rev. Earth Planet. Sci.* 23, 287–336. <https://doi.org/10.1146/annurev.ea.23.050195.001443>.
- Scott, T., Kohlstedt, D., 2006. The effect of large melt fraction on the deformation behavior of peridotite. *Earth Planet. Sci. Lett.* 246, 177–187. <https://doi.org/10.1016/j.epsl.2006.04.027>.
- Sengör, A.M.C., Natal'in, B.A., Burtman, V.S., 1993. Evolution of the Altaiid tectonic collage and Palaeozoic crustal growth in Eurasia. *Nature* 364, 299–307. <https://doi.org/10.1038/364299a0>.
- Spang, A., Baumann, T.S., Kaus, B.J.P., 2021. A Multiphysics Approach to Constrain the Dynamics of the Altiplano-Puna Magmatic System. *J. Geophys. Res. Solid Earth* 126, e2021JB021725. <https://doi.org/10.1029/2021JB021725>.
- Sun, M., Gao, S.S., Liu, K.H., Fu, X., 2020. Upper mantle and mantle transition zone thermal and water content anomalies beneath NE Asia: Constraints from receiver function imaging of the 410 and 660 km discontinuities. *Earth Planet. Sci. Lett.* 532, 116040. <https://doi.org/10.1016/j.epsl.2019.116040>.
- Tape, C., Liu, Q., Maggi, A., Tromp, J., 2010. Seismic tomography of the southern California crust based on spectral-element and adjoint methods. *Geophys. J. Int.* 180, 433–462. <https://doi.org/10.1111/j.1365-246X.2009.04429.x>.
- Tapponnier, P., Molnar, P., 1979. Active faulting and cenozoic tectonics of the Tien Shan, Mongolia, and Baykal Regions. *J. Geophys. Res. Solid Earth* 84, 3425–3459. <https://doi.org/10.1029/JB084iB07p03425>.
- Togtokh, K., Miao, L., Zhang, F., Baatar, M., Anaad, C., Bars, A., 2019. Major, trace element, and Sr–Nd isotopic geochemistry of Cenozoic basalts in Central-North and East Mongolia: Petrogenesis and tectonic implication. *Geol. J.* 54, 3660–3680. <https://doi.org/10.1002/gj.3331>.
- Tong, P., Chen, C., Komatsitsch, D., Basini, P., Liu, Q., 2014. High-resolution seismic array imaging based on an SEM-FK hybrid method. *Geophys. J. Int.* 197, 369–395. <https://doi.org/10.1093/gji/gjt508>.
- Tromp, J., Tape, C., Liu, Q., 2005. Seismic tomography, adjoint methods, time reversal and banana-doughnut kernels: Seismic tomography, adjoint methods, time reversal and banana-doughnut kernels. *Geophys. J. Int.* 160, 195–216. <https://doi.org/10.1111/j.1365-246X.2004.02453.x>.
- Van Der Voo, R., Van Hinsbergen, D.J.J., Domeier, M., Spakman, W., Torsvik, T.H., 2015. Latest Jurassic–earliest Cretaceous closure of the Mongol-Okhotsk Ocean: A paleomagnetic and seismological-tomographic analysis. *Geological Society of America Special Papers*. Geological Society of America, pp. 589–606. [https://doi.org/10.1130/2015.2513\(19\)](https://doi.org/10.1130/2015.2513(19)).
- Van Herwaarden, D., Thrastarson, S., Hapla, V., Afanasiev, M., Trampert, J., Fichtner, A., 2023. Full-Waveform Tomography of the African Plate Using Dynamic Mini-Batches. *J. Geophys. Res. Solid Earth* 128, e2022JB026023. <https://doi.org/10.1029/2022JB026023>.
- Wang, T., Tong, Y., Xiao, W., Guo, L., Windley, B.F., Donskaya, T., Li, S., Tserendash, N., Zhang, J., 2022a. Rollback, scissor-like closure of the Mongol-Okhotsk Ocean and formation of an orocline: magmatic migration based on a large archive of age data. *Natl. Sci. Rev.* 9, nwab210. <https://doi.org/10.1093/nsr/nwab210>.
- Wang, X., Wu, H., Wang, H., Wu, B., Huang, Z., 2022b. Rayleigh wave tomography of central and southern Mongolia. *Tectonophysics* 836, 229426. <https://doi.org/10.1016/j.tecto.2022.229426>.
- Wang, K., Yang, Y., Basini, P., Tong, P., Tape, C., Liu, Q., 2018. Refined crustal and uppermost mantle structure of southern California by ambient noise adjoint tomography. *Geophys. J. Int.* 215, 844–863. <https://doi.org/10.1093/gji/ggy312>.
- Wang, K., Yang, Y., Jiang, C., Wang, Y., Tong, P., Liu, T., Liu, Q., 2021. Adjoint Tomography of Ambient Noise Data and Teleseismic P Waves: Methodology and Applications to Central California. *J. Geophys. Res. Solid Earth* 126. <https://doi.org/10.1029/2021JB021648>.
- Wang, Y., Chevrot, S., Monteiller, V., Komatsitsch, D., Mouthereau, F., Manatschal, G., Sylvander, M., Diaz, J., Ruiz, M., Grimaud, F., Benahmed, S., Pauchet, H., Martin, R., 2016. The deep roots of the western Pyrenees revealed by full waveform inversion of teleseismic P waves. *Geology* 44, 475–478. <https://doi.org/10.1130/G37812.1>.
- Ward, K.M., Zandt, G., Beck, S.L., Christensen, D.H., McFarlin, H., 2014. Seismic imaging of the magmatic underpinnings beneath the Altiplano-Puna volcanic complex from the joint inversion of surface wave dispersion and receiver functions. *Earth Planet. Sci. Lett.* 404, 43–53. <https://doi.org/10.1016/j.epsl.2014.07.022>.
- Windley, B.F., Allen, M.B., 1993. Mongolian plateau: Evidence for a late Cenozoic mantle plume under central Asia. *Geology* 21, 295. [https://doi.org/10.1130/0091-7613\(1993\)021<0295:MPEFAL>2.3.CO;2](https://doi.org/10.1130/0091-7613(1993)021<0295:MPEFAL>2.3.CO;2).
- Xu, M., He, J., 2023. Seispy: Python Module for Batch Calculation and Postprocessing of Receiver Functions. *Seismol. Res. Lett.* 94, 935–943. <https://doi.org/10.1785/0220220288>.
- Xu, M., Wang, K., Chen, J., Yu, D., Tong, P., 2023. Receiver Function Adjoint Tomography for Three-Dimensional High-Resolution Seismic Array Imaging:

- Methodology and Applications in Southeastern Tibet. *Geophys. Res. Lett.* 50, e2023GL104077. <https://doi.org/10.1029/2023GL104077>.
- Xu, Mijian, Huang, Z., Wang, L., Xu, Mingjie, Zhang, Y., Mi, N., Yu, D., Yuan, X., 2020. Sharp Lateral Moho Variations Across the SE Tibetan Margin and Their Implications for Plateau Growth. *J. Geophys. Res. Solid Earth* 125. <https://doi.org/10.1029/2019JB018117>.
- Zhao, H., Wang, P., Huang, Z., 2021. Lithospheric structures beneath the western Mongolian Plateau: Insight from S wave receiver function. *J. Asian Earth Sci.* 212, 104733. <https://doi.org/10.1016/j.jseas.2021.104733>.
- Zhou, Y., Dahlen, F.A., Nolet, G., 2004. Three-dimensional sensitivity kernels for surface wave observables. *Geophys. J. Int.* 158, 142–168. <https://doi.org/10.1111/j.1365-246X.2004.02324.x>.
- Zhu, H., Bozdağ, E., Tromp, J., 2015. Seismic structure of the European upper mantle based on adjoint tomography. *Geophys. J. Int.* 201, 18–52. <https://doi.org/10.1093/gji/ggu492>.